Calibration of the Advanced LIGO detectors for the discovery of the binary black-hole merger GW150914

B. P. Abbott,[1] R. Abbott,[1] T. D. Abbott,[2] M. R. Abernathy,[1] K. Ackley,[3] C. Adams,[4] P. Addesso,[5] R. X. Adhikari,[1] V. B. Adya,[6] C. Affeldt,[6] N. Aggarwal,[7] O. D. Aguiar,[8] A. Ain,[9] P. Ajith,[10] B. Allen,[6,11,12] P. A. Altin,[13] D. V. Amariutei,[3] S. B. Anderson,[1] W. G. Anderson,[11] K. Arai,[1] M. C. Araya,[1] C. C. Arceneaux,[14] J. S. Areeda,[15] K. G. Arun,[16] G. Ashton,[17] M. Ast,[18] S. M. Aston,[4] P. Aufmuth,[12] C. Aulbert,[6] S. Babak,[19] P. T. Baker,[20] S. W. Ballmer,[21] J. C. Barayoga,[1] S. E. Barclay,[22] B. C. Barish,[1] D. Barker,[23] B. Barr,[22] L. Barsotti,[7] J. Bartlett,[23] I. Bartos,[24] R. Bassiri,[25] J. C. Batch,[23] C. Baune,[6] B. Behnke,[19] A. S. Bell,[22] C. J. Bell,[22] B. K. Berger,[1] J. Bergman,[23] G. Bergmann,[6] C. P. L. Berry,[26] J. Betzwieser,[4] S. Bhagwat,[21] R. Bhandare,[27] I. A. Bilenko,[28] G. Billingsley,[1] J. Birch,[4] R. Birney,[29] S. Biscans,[7] A. Bisht,[6,12] C. Biwer,[21] J. K. Blackburn,[1] C. D. Blair,[30] D. Blair,[30] R. M. Blair,[23] O. Bock,[6] T. P. Bodiya,[7] C. Bogan,[6] A. Bohe,[19] P. Bojtos,[31] C. Bond,[26] R. Bork,[1] S. Bose,[32,9] P. R. Brady,[11] V. B. Braginsky,[28] J. E. Brau,[33] M. Brinkmann,[6] P. Brockill,[11] A. F. Brooks,[1] D. A. Brown,[21] D. D. Brown,[26] N. M. Brown,[7] C. C. Buchanan,[2] A. Buikema,[7] A. Buonanno,[19,34] R. L. Byer,[25] L. Cadonati,[35] C. Cahillane,[1] J. Calderón Bustillo,[36,35] T. Callister,[1] J. B. Camp,[37] K. C. Cannon,[38] J. Cao,[39] C. D. Capano,[6] S. Caride,[40] S. Caudill,[11] M. Cavaglià,[14] C. Cepeda,[1] R. Chakraborty,[1] T. Chalermsongsak,[1] S. J. Chamberlin,[11] M. Chan,[22] S. Chao,[41] P. Charlton,[42] H. Y. Chen,[43] Y. Chen,[44] C. Cheng,[41] H. S. Cho,[45] M. Cho,[34] J. H. Chow,[13] N. Christensen,[46] Q. Chu,[30] S. Chung,[30] G. Ciani,[3] F. Clara,[23] J. A. Clark,[35] C. G. Collette,[47] L. Cominsky,[48] M. Constancio Jr.,[8] D. Cook,[23] T. R. Corbitt,[2] N. Cornish,[20] A. Corsi,[49] C. A. Costa,[8] M. W. Coughlin,[46] S. B. Coughlin,[50] S. T. Countryman,[24] P. Couvares,[1] D. M. Coward,[30] M. J. Cowart,[4] D. C. Coyne,[1] R. Coyne,[49] K. Craig,[22] J. D. E. Creighton,[11] J. Cripe,[2] S. G. Crowder,[51] A. Cumming,[22] L. Cunningham,[22] T. Dal Canton,[6] S. L. Danilishin,[22] K. Danzmann,[12,6] N. S. Darman,[52] I. Dave,[27] H. P. Daveloza,[53] G. S. Davies,[22] E. J. Daw,[54] D. DeBra,[25] W. Del Pozzo,[26] T. Denker,[6,12] T. Dent,[6] V. Dergachev,[1] R. DeRosa,[4] R. DeSalvo,[5] S. Dhurandhar,[9] M. C. Díaz,[53] I. Di Palma,[19,6] G. Dojcinoski,[55] F. Donovan,[7] K. L. Dooley,[14] S. Doravari,[4] R. Douglas,[22] T. P. Downes,[11] M. Drago,[6] R. W. P. Drever,[1] J. C. Driggers,[23] Z. Du,[39] S. E. Dwyer,[23] T. B. Edo,[54] M. C. Edwards,[46] A. Effler,[4] H.-B. Eggenstein,[6] P. Ehrens,[1] J. Eichholz,[3] S. S. Eikenberry,[3] W. Engels,[44] R. C. Essick,[7] T. Etzel,[1] M. Evans,[7] T. M. Evans,[4] R. Everett,[56] M. Factourovich,[24] H. Fair,[21] S. Fairhurst,[50] X. Fan,[39] Q. Fang,[30] B. Farr,[43] W. M. Farr,[26] M. Favata,[55] M. Fays,[50] H. Fehrmann,[6] M. M. Fejer,[25] E. C. Ferreira,[8] R. P. Fisher,[21] M. Fletcher,[22] Z. Frei,[31] A. Freise,[26] R. Frey,[33] T. T. Fricke,[6] P. Fritschel,[7] V. V. Frolov,[4] P. Fulda,[3] M. Fyffe,[4] H. A. G. Gabbard,[14] J. R. Gair,[57] S. G. Gaonkar,[9] G. Gaur,[58,59] N. Gehrels,[37] J. George,[27] L. Gergely,[60] A. Ghosh,[10] J. A. Giaime,[2,4] K. D. Giardina,[4] K. Gill,[61] A. Glaefke,[22] E. Goetz,[40] R. Goetz,[3] L. Gondan,[31] G. González,[2] A. Gopakumar,[62] N. A. Gordon,[22] M. L. Gorodetsky,[28] S. E. Gossan,[1] C. Graef,[22] P. B. Graff,[37,34] A. Grant,[22] S. Gras,[7] C. Gray,[23] A. C. Green,[26] H. Grote,[6] S. Grunewald,[19] X. Guo,[39] A. Gupta,[9] M. K. Gupta,[59] K. E. Gushwa,[1] E. K. Gustafson,[1] R. Gustafson,[40] J. J. Hacker,[15] B. R. Hall,[32] E. D. Hall,[1] G. Hammond,[22] M. Haney,[62] M. M. Hanke,[6] J. Hanks,[23] C. Hanna,[56] M. D. Hannam,[50] J. Hanson,[4] T. Hardwick,[2] G. M. Harry,[63] I. W. Harry,[19] M. J. Hart,[22] M. T. Hartman,[3] C.-J. Haster,[26] K. Haughian,[22] M. C. Heintze,[3,4] M. Hendry,[22] I. S. Heng,[22] J. Hennig,[22] A. W. Heptonstall,[1] M. Heurs,[6,12] S. Hild,[22] D. Hoak,[64] K. A. Hodge,[1] S. E. Hollitt,[65] K. Holt,[4] D. E. Holz,[43] P. Hopkins,[50] D. J. Hosken,[65] J. Hough,[22] E. A. Houston,[22] E. J. Howell,[30] Y. M. Hu,[22] S. Huang,[41] E. A. Huerta,[66] B. Hughey,[61] S. Husa,[36] S. H. Huttner,[22] T. Huynh-Dinh,[4] A. Idrisy,[56] N. Indik,[6] D. R. Ingram,[23] R. Inta,[49] H. N. Isa,[22] M. Isi,[1] G. Islas,[15] T. Isogai,[7] B. R. Iyer,[10] K. Izumi,[23] H. Jang,[45] K. Jani,[35] S. Jawahar,[67] F. Jiménez-Forteza,[36] W. W. Johnson,[2] D. I. Jones,[17] R. Jones,[22] L. Ju,[30] Haris K,[68] C. V. Kalaghatgi,[16] V. Kalogera,[69] S. Kandhasamy,[14] G. Kang,[45] J. B. Kanner,[1] S. Karki,[33] M. Kasprzack,[2] E. Katsavounidis,[7] W. Katzman,[4] S. Kaufer,[12] T. Kaur,[30] K. Kawabe,[23] F. Kawazoe,[6] M. S. Kehl,[38] D. Keitel,[6] D. B. Kelley,[21] W. Kells,[1] R. Kennedy,[54] J. S. Key,[53] A. Khalaidovski,[6] F. Y. Khalili,[28] S. Khan,[50] Z. Khan,[59] E. A. Khazanov,[70] N. Kijbunchoo,[23] C. Kim,[45] J. Kim,[71] K. Kim,[72] N. Kim,[45] N. Kim,[25] Y.-M. Kim,[71] E. J. King,[65] P. J. King,[23] D. L. Kinzel,[4] J. S. Kissel,[23] L. Kleybolte,[18] S. Klimenko,[3] S. M. Koehlenbeck,[6] K. Kokeyama,[2] V. Kondrashov,[1] A. Kontos,[7] M. Korobko,[18] W. Z. Korth,[1] D. B. Kozak,[1] V. Kringel,[6] C. Krueger,[12] G. Kuehn,[6] P. Kumar,[38] L. Kuo,[41] B. D. Lackey,[21] M. Landry,[23] J. Lange,[73] B. Lantz,[25] P. D. Lasky,[74] A. Lazzarini,[1] C. Lazzaro,[35] P. Leaci,[19] S. Leavey,[22] E. O. Lebigot,[39] C. H. Lee,[71] H. K. Lee,[72] H. M. Lee,[75] K. Lee,[22] A. Lenon,[21] J. R. Leong,[6] Y. Levin,[74] B. M. Levine,[23] T. G. F. Li,[1] A. Libson,[7] T. B. Littenberg,[76] N. A. Lockerbie,[67] J. Logue,[22] A. L. Lombardi,[64] J. E. Lord,[21] M. Lormand,[4] J. D. Lough,[6,12] H. Lück,[12,6] A. P. Lundgren,[6] J. Luo,[46] R. Lynch,[7] Y. Ma,[30] T. MacDonald,[25] B. Machenschalk,[6] M. MacInnis,[7] D. M. Macleod,[2] F. Magaña-Sandoval,[21] R. M. Magee,[32] M. Mageswaran,[1] I. Mandel,[26] V. Mandic,[51] V. Mangano,[22] G. L. Mansell,[13] M. Manske,[11] S. Márka,[24] Z. Márka,[24] A. S. Markosyan,[25] E. Maros,[1] I. W. Martin,[22] R. M. Martin,[3] D. V. Martynov,[1] J. N. Marx,[1] K. Mason,[7] T. J. Massinger,[21] M. Masso-Reid,[22] F. Matichard,[7] L. Matone,[24] N. Mavalvala,[7] N. Mazumder,[32] G. Mazzolo,[6] R. McCarthy,[23] D. E. McClelland,[13] S. McCormick,[4] S. C. McGuire,[77] G. McIntyre,[1] J. McIver,[64] D. J. McManus,[13] S. T. McWilliams,[66] G. D. Meadors,[19,6] A. Melatos,[52] G. Mendell,[23] D. Mendoza-Gandara,[6] R. A. Mercer,[11] E. Merilh,[23] S. Meshkov,[1] C. Messenger,[22] C. Messick,[56] P. M. Meyers,[51] H. Miao,[26] H. Middleton,[26] E. E. Mikhailov,[78] K. N. Mukund,[9] J. Miller,[7] M. Millhouse,[20] J. Ming,[19,6] S. Mirshekari,[79] C. Mishra,[10] S. Mitra,[9] V. P. Mitrofanov,[28]

G. Mitselmakher,[3] R. Mittleman,[7] S. R. P. Mohapatra,[7] B. C. Moore,[55] C. J. Moore,[80] D. Moraru,[23] G. Moreno,[23] S. R. Morriss,[53] K. Mossavi,[6] C. M. Mow-Lowry,[26] C. L. Mueller,[3] G. Mueller,[3] A. W. Muir,[50] Arunava Mukherjee,[10] D. Mukherjee,[11] S. Mukherjee,[53] A. Mullavey,[4] J. Munch,[65] D. J. Murphy,[24] P. G. Murray,[22] A. Mytidis,[3] R. K. Nayak,[81] V. Necula,[3] K. Nedkova,[64] A. Neunzert,[40] G. Newton,[22] T. T. Nguyen,[13] A. B. Nielsen,[6] A. Nitz,[6] D. Nolting,[4] M. E. N. Normandin,[53] L. K. Nuttall,[21] J. Oberling,[23] E. Ochsner,[11] J. O'Dell,[82] E. Oelker,[7] G. H. Ogin,[83] J. J. Oh,[84] S. H. Oh,[84] F. Ohme,[50] M. Oliver,[36] P. Oppermann,[6] Richard J. Oram,[4] B. O'Reilly,[4] R. O'Shaughnessy,[73] C. D. Ott,[44] D. J. Ottaway,[65] R. S. Ottens,[3] H. Overmier,[4] B. J. Owen,[49] A. Pai,[68] S. A. Pai,[27] J. R. Palamos,[33] O. Palashov,[70] A. Pal-Singh,[18] H. Pan,[41] C. Pankow,[11,69] F. Pannarale,[50] B. C. Pant,[27] M. A. Papa,[19,11,6] H. R. Paris,[25] W. Parker,[4] D. Pascucci,[22] Z. Patrick,[25] B. L. Pearlstone,[22] M. Pedraza,[1] L. Pekowsky,[21] A. Pele,[4] S. Penn,[85] R. Pereira,[24] A. Perreca,[1] M. Phelps,[22] V. Pierro,[5] I. M. Pinto,[5] M. Pitkin,[22] A. Post,[6] J. Powell,[22] J. Prasad,[9] V. Predoi,[50] S. S. Premachandra,[74] T. Prestegard,[51] L. R. Price,[1] M. Principe,[5] S. Privitera,[19] L. Prokhorov,[28] O. Puncken,[6] M. Pürrer,[50] H. Qi,[11] J. Qin,[30] V. Quetschke,[53] E. A. Quintero,[1] R. Quitzow-James,[33] F. J. Raab,[23] D. S. Rabeling,[13] H. Radkins,[23] P. Raffai,[31] S. Raja,[27] M. Rakhmanov,[53] V. Raymond,[19] J. Read,[15] C. M. Reed,[23] S. Reid,[29] D. H. Reitze,[1,3] H. Rew,[78] K. Riles,[40] N. A. Robertson,[1,22] R. Robie,[22] J. G. Rollins,[1] V. J. Roma,[33] G. Romanov,[78] J. H. Romie,[4] S. Rowan,[22] A. Rüdiger,[6] K. Ryan,[23] S. Sachdev,[1] T. Sadecki,[23] L. Sadeghian,[11] M. Saleem,[68] F. Salemi,[6] A. Samajdar,[81] L. Sammut,[52,74] E. J. Sanchez,[1] V. Sandberg,[23] B. Sandeen,[69] J. R. Sanders,[40] B. S. Sathyaprakash,[50] P. R. Saulson,[21] O. Sauter,[40] R. L. Savage,[23] A. Sawadsky,[12] P. Schale,[33] R. Schilling†,[6] J. Schmidt,[6] P. Schmidt,[1,44] R. Schnabel,[18] R. M. S. Schofield,[33] A. Schönbeck,[18] E. Schreiber,[6] D. Schuette,[6,12] B. F. Schutz,[50] J. Scott,[22] S. M. Scott,[13] D. Sellers,[4] A. Sergeev,[70] G. Serna,[15] A. Sevigny,[23] D. A. Shaddock,[13] M. S. Shahriar,[69] M. Shaltev,[6] Z. Shao,[1] B. Shapiro,[25] P. Shawhan,[34] A. Sheperd,[11] D. H. Shoemaker,[7] D. M. Shoemaker,[35] X. Siemens,[11] D. Sigg,[23] A. D. Silva,[8] D. Simakov,[6] A. Singer,[1] L. P. Singer,[37] A. Singh,[19,6] R. Singh,[2] A. M. Sintes,[36] B. J. J. Slagmolen,[13] J. R. Smith,[15] N. D. Smith,[1] R. J. E. Smith,[1] E. J. Son,[84] B. Sorazu,[22] T. Souradeep,[9] A. K. Srivastava,[59] A. Staley,[24] M. Steinke,[6] J. Steinlechner,[22] S. Steinlechner,[22] D. Steinmeyer,[6,12] B. C. Stephens,[11] R. Stone,[53] K. A. Strain,[22] N. A. Strauss,[46] S. Strigin,[28] R. Sturani,[79] A. L. Stuver,[4] T. Z. Summerscales,[86] L. Sun,[52] P. J. Sutton,[50] M. J. Szczepańczyk,[61] D. Talukder,[33] D. B. Tanner,[3] M. Tápai,[60] S. P. Tarabrin,[6] A. Taracchini,[19] R. Taylor,[1] T. Theeg,[6] M. P. Thirugnanasambandam,[1] E. G. Thomas,[26] M. Thomas,[4] P. Thomas,[23] K. A. Thorne,[4] K. S. Thorne,[44] E. Thrane,[74] V. Tiwari,[50] K. V. Tokmakov,[67] C. Tomlinson,[54] C. V. Torres‡,[53] C. I. Torrie,[1] D. Töyrä,[26] G. Traylor,[4] D. Trifirò,[14] M. Tse,[7] D. Tuyenbayev,[53] D. Ugolini,[87] C. S. Unnikrishnan,[62] A. L. Urban,[11] S. A. Usman,[21] H. Vahlbruch,[12] G. Vajente,[1] G. Valdes,[53] D. C. Vander-Hyde,[21,15] A. A. van Veggel,[22] S. Vass,[1] R. Vaulin,[7] A. Vecchio,[26] J. Veitch,[26] P. J. Veitch,[65] K. Venkateswara,[88] S. Vinciguerra,[26] D. J. Vine,[29] S. Vitale,[7] T. Vo,[21] C. Vorvick,[23] W. D. Vousden,[26] S. P. Vyatchanin,[28] A. R. Wade,[13] L. E. Wade,[89] M. Wade,[89] M. Walker,[2] L. Wallace,[1] S. Walsh,[11] H. Wang,[26] M. Wang,[26] X. Wang,[39] Y. Wang,[30] R. L. Ward,[13] J. Warner,[23] B. Weaver,[23] M. Weinert,[6] A. J. Weinstein,[1] R. Weiss,[7] T. Welborn,[4] L. Wen,[30] P. Weßels,[6] T. Westphal,[6] K. Wette,[6] J. T. Whelan,[73,6] D. J. White,[54] B. F. Whiting,[3] R. D. Williams,[1] A. R. Williamson,[50] J. L. Willis,[90] B. Willke,[12,6] M. H. Wimmer,[6,12] W. Winkler,[6] C. C. Wipf,[1] H. Wittel,[6,12] G. Woan,[22] J. Worden,[23] J. L. Wright,[22] G. Wu,[4] J. Yablon,[69] W. Yam,[7] H. Yamamoto,[1] C. C. Yancey,[34] M. J. Yap,[13] H. Yu,[7] M. Zanolin,[61] M. Zevin,[69] F. Zhang,[7] L. Zhang,[1] M. Zhang,[78] Y. Zhang,[73] C. Zhao,[30] M. Zhou,[69] Z. Zhou,[69] X. J. Zhu,[30] M. E. Zucker,[1,7] S. E. Zuraw,[64] and J. Zweizig[1]

†Deceased, May 2015. ‡Deceased, March 2015.

(LIGO Scientific Collaboration)*

[1]*LIGO, California Institute of Technology, Pasadena, CA 91125, USA*
[2]*Louisiana State University, Baton Rouge, LA 70803, USA*
[3]*University of Florida, Gainesville, FL 32611, USA*
[4]*LIGO Livingston Observatory, Livingston, LA 70754, USA*
[5]*University of Sannio at Benevento, I-82100 Benevento, Italy and INFN, Sezione di Napoli, I-80100 Napoli, Italy*
[6]*Albert-Einstein-Institut, Max-Planck-Institut für Gravitationsphysik, D-30167 Hannover, Germany*
[7]*LIGO, Massachusetts Institute of Technology, Cambridge, MA 02139, USA*
[8]*Instituto Nacional de Pesquisas Espaciais, 12227-010 São José dos Campos, SP, Brazil*
[9]*Inter-University Centre for Astronomy and Astrophysics, Pune 411007, India*
[10]*International Centre for Theoretical Sciences, Tata Institute of Fundamental Research, Bangalore 560012, India*
[11]*University of Wisconsin-Milwaukee, Milwaukee, WI 53201, USA*
[12]*Leibniz Universität Hannover, D-30167 Hannover, Germany*
[13]*Australian National University, Canberra, Australian Capital Territory 0200, Australia*
[14]*The University of Mississippi, University, MS 38677, USA*
[15]*California State University Fullerton, Fullerton, CA 92831, USA*
[16]*Chennai Mathematical Institute, Chennai, India*
[17]*University of Southampton, Southampton SO17 1BJ, United Kingdom*
[18]*Universität Hamburg, D-22761 Hamburg, Germany*
[19]*Albert-Einstein-Institut, Max-Planck-Institut für Gravitationsphysik, D-14476 Potsdam-Golm, Germany*

[20]*Montana State University, Bozeman, MT 59717, USA*
[21]*Syracuse University, Syracuse, NY 13244, USA*
[22]*SUPA, University of Glasgow, Glasgow G12 8QQ, United Kingdom*
[23]*LIGO Hanford Observatory, Richland, WA 99352, USA*
[24]*Columbia University, New York, NY 10027, USA*
[25]*Stanford University, Stanford, CA 94305, USA*
[26]*University of Birmingham, Birmingham B15 2TT, United Kingdom*
[27]*RRCAT, Indore MP 452013, India*
[28]*Faculty of Physics, Lomonosov Moscow State University, Moscow 119991, Russia*
[29]*SUPA, University of the West of Scotland, Paisley PA1 2BE, United Kingdom*
[30]*University of Western Australia, Crawley, Western Australia 6009, Australia*
[31]*MTA Eötvös University, "Lendulet" Astrophysics Research Group, Budapest 1117, Hungary*
[32]*Washington State University, Pullman, WA 99164, USA*
[33]*University of Oregon, Eugene, OR 97403, USA*
[34]*University of Maryland, College Park, MD 20742, USA*
[35]*Center for Relativistic Astrophysics and School of Physics, Georgia Institute of Technology, Atlanta, GA 30332, USA*
[36]*Universitat de les Illes Balears, IAC3—IEEC, E-07122 Palma de Mallorca, Spain*
[37]*NASA/Goddard Space Flight Center, Greenbelt, MD 20771, USA*
[38]*Canadian Institute for Theoretical Astrophysics, University of Toronto, Toronto, Ontario M5S 3H8, Canada*
[39]*Tsinghua University, Beijing 100084, China*
[40]*University of Michigan, Ann Arbor, MI 48109, USA*
[41]*National Tsing Hua University, Hsinchu City, Taiwan 30013, R.O.C.*
[42]*Charles Sturt University, Wagga Wagga, New South Wales 2678, Australia*
[43]*University of Chicago, Chicago, IL 60637, USA*
[44]*Caltech CaRT, Pasadena, CA 91125, USA*
[45]*Korea Institute of Science and Technology Information, Daejeon 305-806, Korea*
[46]*Carleton College, Northfield, MN 55057, USA*
[47]*University of Brussels, Brussels 1050, Belgium*
[48]*Sonoma State University, Rohnert Park, CA 94928, USA*
[49]*Texas Tech University, Lubbock, TX 79409, USA*
[50]*Cardiff University, Cardiff CF24 3AA, United Kingdom*
[51]*University of Minnesota, Minneapolis, MN 55455, USA*
[52]*The University of Melbourne, Parkville, Victoria 3010, Australia*
[53]*The University of Texas Rio Grande Valley, Brownsville, TX 78520, USA*
[54]*The University of Sheffield, Sheffield S10 2TN, United Kingdom*
[55]*Montclair State University, Montclair, NJ 07043, USA*
[56]*The Pennsylvania State University, University Park, PA 16802, USA*
[57]*School of Mathematics, University of Edinburgh, Edinburgh EH9 3FD, United Kingdom*
[58]*Indian Institute of Technology, Gandhinagar Ahmedabad Gujarat 382424, India*
[59]*Institute for Plasma Research, Bhat, Gandhinagar 382428, India*
[60]*University of Szeged, Dóm tér 9, Szeged 6720, Hungary*
[61]*Embry-Riddle Aeronautical University, Prescott, AZ 86301, USA*
[62]*Tata Institute of Fundamental Research, Mumbai 400005, India*
[63]*American University, Washington, D.C. 20016, USA*
[64]*University of Massachusetts-Amherst, Amherst, MA 01003, USA*
[65]*University of Adelaide, Adelaide, South Australia 5005, Australia*
[66]*West Virginia University, Morgantown, WV 26506, USA*
[67]*SUPA, University of Strathclyde, Glasgow G1 1XQ, United Kingdom*
[68]*IISER-TVM, CET Campus, Trivandrum Kerala 695016, India*
[69]*Northwestern University, Evanston, IL 60208, USA*
[70]*Institute of Applied Physics, Nizhny Novgorod, 603950, Russia*
[71]*Pusan National University, Busan 609-735, Korea*
[72]*Hanyang University, Seoul 133-791, Korea*
[73]*Rochester Institute of Technology, Rochester, NY 14623, USA*
[74]*Monash University, Victoria 3800, Australia*
[75]*Seoul National University, Seoul 151-742, Korea*
[76]*University of Alabama in Huntsville, Huntsville, AL 35899, USA*
[77]*Southern University and A&M College, Baton Rouge, LA 70813, USA*
[78]*College of William and Mary, Williamsburg, VA 23187, USA*
[79]*Instituto de Física Teórica, University Estadual Paulista/ICTP South American Institute for Fundamental Research, São Paulo SP 01140-070, Brazil*
[80]*University of Cambridge, Cambridge CB2 1TN, United Kingdom*
[81]*IISER-Kolkata, Mohanpur, West Bengal 741252, India*

[82]Rutherford Appleton Laboratory, HSIC, Chilton, Didcot, Oxon OX11 0QX, United Kingdom
[83]Whitman College, 280 Boyer Ave, Walla Walla, WA 9936, USA
[84]National Institute for Mathematical Sciences, Daejeon 305-390, Korea
[85]Hobart and William Smith Colleges, Geneva, NY 14456, USA
[86]Andrews University, Berrien Springs, MI 49104, USA
[87]Trinity University, San Antonio, TX 78212, USA
[88]University of Washington, Seattle, WA 98195, USA
[89]Kenyon College, Gambier, OH 43022, USA
[90]Abilene Christian University, Abilene, TX 79699, USA

In Advanced LIGO, detection and astrophysical source parameter estimation of the binary black hole merger GW150914 requires a calibrated estimate of the gravitational-wave strain sensed by the detectors. Producing an estimate from each detector's differential arm length control loop readout signals requires applying time domain filters, which are designed from a frequency domain model of the detector's gravitational-wave response. The gravitational-wave response model is determined by the detector's opto-mechanical response and the properties of its feedback control system. The measurements used to validate the model and characterize its uncertainty are derived primarily from a dedicated photon radiation pressure actuator, with cross-checks provided by optical and radio frequency references. We describe how the gravitational-wave readout signal is calibrated into equivalent gravitational-wave-induced strain and how the statistical uncertainties and systematic errors are assessed. Detector data collected over 38 calendar days, from September 12 to October 20, 2015, contain the event GW150914 and approximately 16 days of coincident data used to estimate the event false alarm probability. The calibration uncertainty is less than 10% in magnitude and 10° in phase across the relevant frequency band 20 Hz to 1 kHz.

PACS numbers: 04.30.-w, 04.80.Nn, 95.55.Ym

I. INTRODUCTION

On September 14, 2015 09:50:45 UTC, the two Advanced LIGO detectors observed a gravitational-wave (GW) signal, GW150914, originating from the merging of two stellar-mass black holes [1]. The event was observed in coincident data from the two LIGO detectors between September 12 to October 20, 2015. These detectors, H1 located on the Hanford Reservation in Richland, Washington, and L1 located in Livingston Parish, Louisiana, are laser interferometers [2] that use four mirrors (referred to as test masses) suspended from multi-stage pendulums to form two perpendicular optical cavities (arms) in a modified Michelson configuration, as shown in Fig. 1. GW strain causes apparent differential variations of the arm lengths which generate power fluctuations in the interferometer's GW readout port. These power fluctuations, measured by photodiodes, serve as both the GW readout signal and an error signal for controlling the differential arm length [3].'

Feedback control of the differential arm length degree of freedom (along with the interferometer's other length and angular degrees of freedom) is required for stable operation of the instrument. This control is achieved by taking a digitized version of the GW readout signal $d_{\rm err}(f)$, applying a set of digital filters to produce a control signal $d_{\rm ctrl}(f)$, then sending the control signal to the test mass actuator systems which displace the mirrors. Without this control system, differential length variations arising from either displacement noise or a passing GW would cause an unsuppressed (free-running) change in differential length, $\Delta L_{\rm free} = L_x - L_y = hL$, where $L \equiv (L_x + L_y)/2$ is the average length of each detector's arms, with lengths L_x and L_y, and h is the sensed strain, $h \equiv \Delta L_{\rm free}/L$. In the presence of feedback control, however, this free-running displacement is suppressed to a smaller, residual length change given by $\Delta L_{\rm res} = \Delta L_{\rm free}(f)/[1 + G(f)]$, where $G(f)$ is the open loop transfer function of the differential arm length servo. Therefore, estimating the equivalent GW strain sensed by the interferometer requires detailed characterization of, and correction for, the effect of this loop. The effects of other feedback loops associated with other degrees of freedom are negligible across the relevant frequency band, from 20 Hz to 1 kHz.

The differential arm length feedback loop is characterized by a sensing function $C(f)$, a digital filter function $D(f)$, and an actuation function $A(f)$, which together give the open loop transfer function

$$G(f) = A(f)\,D(f)\,C(f)\,. \tag{1}$$

The sensing function describes how residual arm length displacements propagate to the digitized error signal, $d_{\rm err}(f) \equiv C(f)\,\Delta L_{\rm res}(f)$; the digital filter function describes how the digital control signal is generated from the digital error signal, $d_{\rm ctrl}(f) \equiv D(f)\,d_{\rm err}(f)$; and the actuation function describes how the digital control signal produces a differential displacement of the arm lengths, $\Delta L_{\rm ctrl} \equiv A(f)\,d_{\rm ctrl}(f)$. These relationships are shown schematically in Fig. 2.

Either the error signal, the control signal, or a combination of the two can be used estimate the strain sensed by the detector [4]. For Advanced LIGO, a combination was chosen that renders the estimate of the detector strain output insensitive to changes in the digital filter function D, and makes application of slow corrections to the sensing and actuation functions convenient:

$$h(t) = \frac{1}{L}\left[C^{-1} * d_{\rm err}(t) + \mathcal{A} * d_{\rm ctrl}(t)\right]\,, \tag{2}$$

where $\mathcal{A}$ and C^{-1} are time domain filters generated from frequency domain models of A and C, and $*$ denotes convolution.

* Corresponding Author: spokesperson@ligo.org

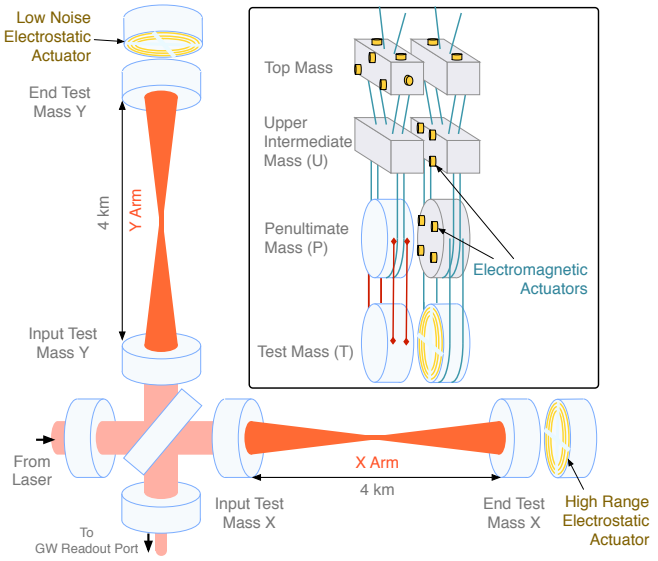

FIG. 1. Simplified diagram of an Advanced LIGO interferometer. Four highly reflective test masses form two Fabry–Pérot arm cavities. At lower left, a power recycling mirror placed between the laser and the beamsplitter increases the power stored in the arms to 100 kW. A signal recycling mirror, placed between the beamsplitter and the GW readout photodetector, alters the frequency response of the interferometer to differential arm length fluctuations. For clarity, only the lowest suspension stage is shown for the optics. Inset: one of the dual-chain, quadruple pendulum suspension systems is shown.

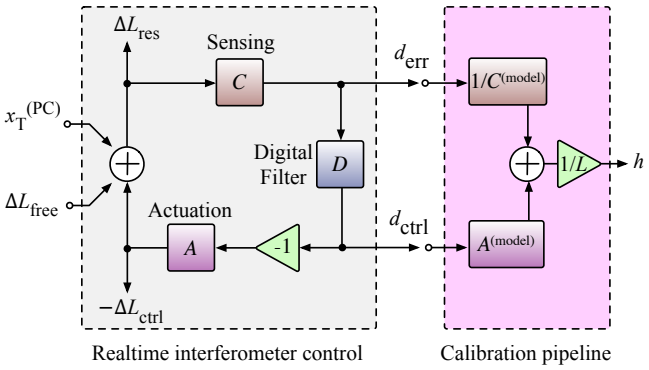

FIG. 2. Block diagram of the differential arm length feedback control servo. The sensing function, digital filter function, and actuation function combine to form the open loop transfer function $G(f) = A(f)\,D(f)\,C(f)$. The signal $x_T^{(PC)}$ is described in section IV.

The accuracy and precision of this estimated strain rely on characterizing the sensing and actuation functions of each detector, C and A. Each function is represented by a model, generated from measurements of control loop parameters, each with associated statistical uncertainty and systematic error. Uncertainty in the calibration model parameters directly impacts the uncertainty in the reconstructed detector strain signal. This uncertainty could limit the signal-to-noise ratios of GW detection statistics, and could dominate uncertainties in estimated astrophysical parameters, e.g., luminosity distance, sky location, component masses, and spin. Calibration uncertainty is thus crucial for GW searches and parameter estimation.

This paper describes the accuracy and precision of the model parameters and of the estimated detector strain output over the course of the 38 calendar days of observation during which GW150914 was detected. Sec. II describes the actuation and sensing function models in terms of their measured parameters. Sec. III defines the treatment of uncertainty and error for each of these parameters. In Sec. IV, a description of the radiation pressure actuator is given. Secs. V and VI discuss the measurements used to determine the static statistical uncertainties and systematic errors in the actuation and sensing function models, respectively, and their results. Sec. VII details the systematic errors in model parameters near the time of the GW150914 event resulting from uncorrected, slow time variations. Sec. VIII discusses each detector's strain response function that is used to estimate the overall amplitude and phase uncertainties and systematic errors in the calibrated data stream $h(t)$. Sec. IX discusses the inter-site uncertainty in the relative timing of each detector's data stream. In Sec. X the implications of these uncertainties on the detection and astrophysical parameter estimation of GW150914 are summarized. Finally, in Sec. XI we give an outlook on future calibration and its role in GW detection and astrophysical parameter estimation.

II. MODEL DESCRIPTION

We divide the differential arm length feedback loop into two main functions, sensing and actuation. In this section, these functions are described in detail. The interferometer response function is also introduced; it is composed of these functions and the digital control filter function (which is precisely known and carries no uncertainty), and is useful for estimating the overall uncertainty in the estimated strain.

A. Sensing function

The sensing function C describes the interferometric response of the detector. It converts residual test mass differential displacement ΔL_{res} to the signal at the GW readout port. The sensing function includes the response of the photodiodes, their analog readout electronics, and effects from the digitization process, all of which convert GW port laser power variations to counts (ct) of digital signal d_{err}, sampled at a rate of 16 384 Hz.

The interferometric response is determined by the arm cavity mirror (test mass) reflectivities, the reflectivity of the signal recycling mirror (see Fig. 1), the length of the arm cavities and the length of the signal recycling cavity [5, 6]. The response is well approximated by a single-pole low-pass filter with a gain and an additional time delay.

The sensing function is thus given by

$$C^{(\mathrm{model})}(f) = \frac{\mathcal{K}_C}{1 + \mathrm{i}f/f_C}\, C_R(f)\, \exp(-2\pi \mathrm{i} f \tau_C)\,, \qquad (3)$$

where $\mathcal{K}_C$ is combined gain of the opto-mechanical response and analog-to-digital converter (see Fig. 3). It describes, at

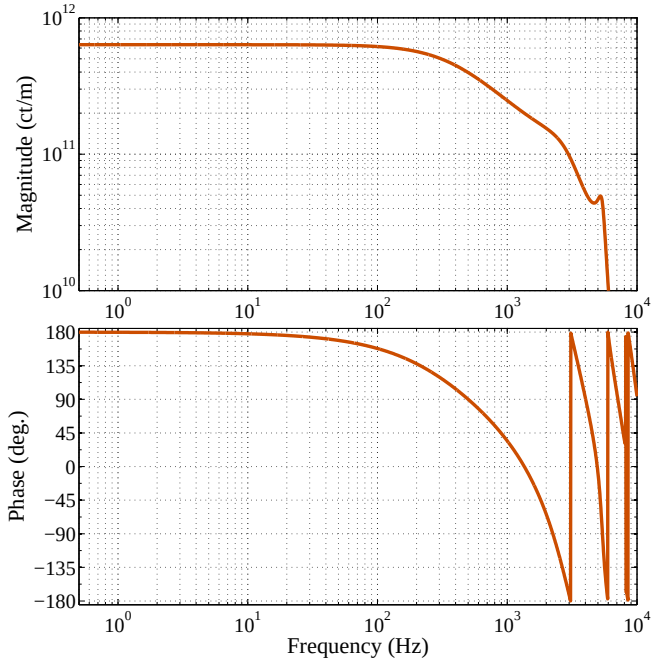

FIG. 3. The magnitude and phase of the sensing function model $C(f)$ for the L1 detector. Below 1 kHz the frequency dependence is determined by f_C, while above 1 kHz it is determined by the analog-to-digital conversion process.

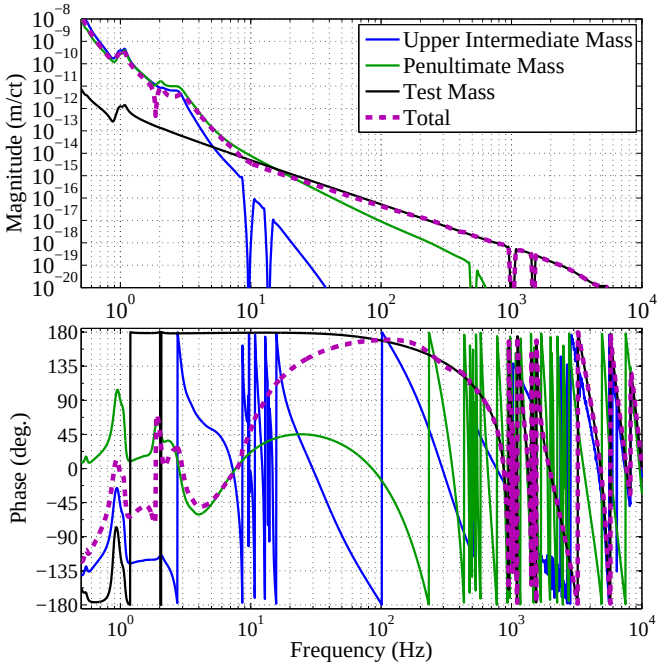

FIG. 4. Overall actuation transfer function $A(f)$ and actuation functions for each suspension stage $F_i(f)\,\mathcal{K}_i\,A_i(f)$ for the L1 detector. The mechanical response of the pendulums and F_i dictate the characteristics of each stage. The strongest actuator, that for the upper intermediate mass, is used below a few Hz. Above ~30 Hz, only the test mass actuator is used. At certain frequencies (e.g., 10, 14, and 500 Hz), digital notch filters are implemented for high quality factor features of the pendulum responses in order to avoid mechanical instabilities. The H1 actuation function differs slightly in scale, frequency dependence, and digital filter choice.

a reference time, how many digital counts are produced in $d_{\rm err}$ in response to differential arm length displacement. The pole frequency, f_C (341 Hz and 388 Hz for H1 and L1, respectively), is the characteristic frequency that describes the attenuation of the interferometer response to high-frequency length perturbations [5]. The time delay τ_C includes the light travel time L/c along the length of the arms (L = 3994.5 m), computational delay in the digital acquisition system, and the delay introduced to approximate the complete interferometric response as a single pole. Finally, the dimensionless quantity $C_R(f)$ accounts for any additional frequency dependence of the sensing function. It has features, mostly above 1 kHz, arising from the properties of the photodiode electronics, as well as analog and digital signal processing filters.

B. Actuation function

The interferometer differential arm length can be controlled by actuating on the quadruple suspension system for any of the four arm cavity test masses. Each of these systems consists of four stages, suspended as cascading pendulums [7, 8], which isolate the test mass from residual motion of the supporting active isolation system [9]. Each suspension system also includes an adjacent, nearly-identical, cascaded reaction mass pendulum chain which can be used to independently generate reaction forces on each mass of the test mass pendulum chain. A diagram of one of these suspension systems is shown in Fig. 1.

For each of the three lowest stages of the suspension system—the upper intermediate mass (U), the penultimate mass (P), and the test mass (T)—digital-to-analog converters and associated electronics drive a set of four actuators that work in concert to displace each stage, and consequently the test mass suspended at the bottom. The digital control signal $d_{\rm ctrl}$ is distributed to each stage and multiplied by a set of dimensionless digital filters $F_i(f)$, where i = U, P, or T, so that the lower stages are used for the highest frequency signal content and the upper stages are used for high-range, low-frequency signal content.

While the differential arm length can be controlled using any combination of the four test mass suspension systems, only one, the Y-arm end test mass, is used to create $\Delta L_{\rm ctrl}$. Actuating a single test mass affects both the common and the differential arm lengths. The common arm length change is compensated, however, by high-bandwidth (~14 kHz) feedback to the laser frequency.

The model of the actuation function A of the suspension system comprises the mechanical dynamics, electronics, and digital filtering, and is written as

$$A^{(\rm model)}(f) = \Big[F_{\rm T}(f)\,\mathcal{K}_{\rm T}\,A_{\rm T}(f) + F_{\rm P}(f)\,\mathcal{K}_{\rm P}\,A_{\rm P}(f) + F_{\rm U}(f)\,\mathcal{K}_{\rm U}\,A_{\rm U}(f)\Big]\,\exp(-2\pi {\rm i} f \tau_A)\,. \quad (4)$$

Here $\mathcal{K}_i$ and $A_i(f)$ are the gain and the normalized frequency dependence of the ith suspension stage actuator, measured at a

reference time, that define the actuation transfer function for each suspension stage; τ_A is the computational delay in the digital-to-analog conversion. The overall and individual stage actuation functions are plotted as a function of frequency in Fig. 4. The gain converts voltage applied at suspension stage i to test mass displacement. The frequency response is primarily determined by the mechanical dynamics of the suspension, but also includes minor frequency dependent terms from digital-to-analog signal processing, analog electronics, and mechanical interaction with the locally-controlled suspension stage for the top mass (see Fig. 1). While opto-mechanical interaction from radiation pressure can affect the actuation function [10], the laser power resonating in the arm cavities during the observation period was low enough that radiation pressure effects can be ignored. The H1 and L1 suspensions and electronics are identical by design, but there are slight differences, mostly due to the digital filtering for each stage F_i, which are precisely known and carry no uncertainty.

C. Response function

For uncertainty estimation, it is convenient to introduce the response function $R(f)$ that relates the differential arm length servo error signal to strain sensed by the interferometer: $h(f) = (1/L)\,R(f)\,d_{\rm err}(f)$. As shown schematically in Fig. 2, the response function is given by

$$R(f) = \frac{1 + A(f)\,D(f)\,C(f)}{C(f)} = \frac{1 + G(f)}{C(f)}\,. \tag{5}$$

We will use this response function to evaluate the overall accuracy and precision of the calibrated detector strain output. The actuation function dominates at frequencies below the differential arm length servo unity gain frequency, 40 Hz and 56 Hz for H1 and L1, respectively. Above the unity gain frequency, the sensing function dominates (see Figs. 3 and 4).

III. DEFINITIONS OF PARAMETER UNCERTAINTY

Using Eqs. (3) and (4) we identify the set Q of parameters that must be characterized in order to define the sensing and actuation functions (see Table I). The remaining parameters, $F_i(f)$ and τ_A, are part of the digital control system and thus known with negligible uncertainty.

Combinations of these scalar and frequency dependent parameters form a set $Q_{\rm meas}$ of measurable quantities:

$$\begin{aligned} Q_{\rm meas} = \{&\mathcal{K}_{\rm T}A_{\rm T}(f), \mathcal{K}_{\rm P}A_{\rm P}(f), \mathcal{K}_{\rm U}A_{\rm U}(f), \\ &\mathcal{K}_{\rm C}C_{\rm R}(f)/(1 + {\rm i}f/f_{\rm C})\}\,, \end{aligned} \tag{6}$$

where each element includes its associated time delay $\tau_{\rm A}$ or $\tau_{\rm C}$. Each quantity $q_{\rm meas} \in Q_{\rm meas}$ is measured using sinusoidal excitations injected at various points in the control loop while the detector is in its lowest noise state. Each measurement consists of excitations that are injected consecutively at discrete frequencies. Measurements made at a reference time t_0 are used to construct a model q_0 for $q_{\rm meas}$. The models contain

TABLE I. The set of differential arm length control loop parameters that must be characterized to define the sensing and actuation functions.

Parameter	Description
$A_{\rm T}(f)$	Normalized test mass actuation function
$A_{\rm P}(f)$	Normalized penultimate mass actuation function
$A_{\rm U}(f)$	Normalized upper intermediate mass actuation function
$C_{\rm R}(f)$	Residual sensing function frequency dependence
$\mathcal{K}_C$	Sensing function gain
$\mathcal{K}_{\rm T}$	Test mass actuation function gain
$\mathcal{K}_{\rm P}$	Penultimate mass actuation function gain
$\mathcal{K}_{\rm U}$	Upper intermediate mass actuation function gain
f_C	Cavity pole frequency
τ_C	Sensing function time delay

frequency-dependent statistical uncertainty derived from the coherence $\gamma^2(f)$ between excitation and response during the measurements. At each frequency, the standard deviation σ_{q_0} (i.e., the 68% confidence interval) of q_0 is given by

$$\sigma_{q_0}(f) = \left[\frac{1 - \gamma^2(f)}{2N\gamma^2(f)}\right]^{1/2}\,, \tag{7}$$

where N is the number of measurements performed at each frequency point [11]. The measurements are repeated at different times to validate and refine the estimates of $\sigma_{q_0}(f)$.

Where a reference model q_0 does not completely describe the frequency dependence in a measured quantity $q_{\rm meas}$, we use the difference between the model and the measurements to define a known, complex systematic error $\delta q = q_{\rm meas} - q_0$. For most parameters, instead of dealing directly with the known systematic error δq, it is convenient to work with the complex quantity $1 + \delta q/q_0 = q_{\rm meas}/q_0$. This is the systematic error expressed as a multiplicative correction factor in the frequency domain which must be applied to q_0 in order to obtain the measured value $q_{\rm meas}$. The estimate of δq, which also includes additional measurements made after the reference time, has a statistical uncertainty $\sigma_{\delta q}(f)$. This uncertainty is informed by the covariance of a low-order spline fit to the frequency-dependent correction factor. The variance of the ratio of the measured correction factors to the modeled fit is computed and added together with $\sigma^2_{\delta q}(f)$ to form the statistical uncertainty of the fit.

In total, the frequency-dependent estimate of q is

$$q(f) = q_0(f) + \delta q(f) \pm \left[\sigma^2_{q_0}(f) + \sigma^2_{\delta q}(f)\right]^{1/2}\,, \tag{8}$$

where we assume that statistical uncertainties in q_0 and δq result from Gaussian distributions with zero mean and standard deviations σ_{q_0} and $\sigma_{\delta q}$, respectively.

The frequency-independent parameters $\mathcal{K}_i$ and $f_{\rm C}$ are monitored continuously during data taking to track small, slow variations. Tracking is achieved using a set of sinusoidal excitations at select frequencies, typically referred to as *calibration lines*. The observed time-dependence in $\mathcal{K}_i$ and $f_{\rm C}$ is treated as a systematic error $\delta q(t)$ with an associated statistical uncertainty $\sigma_{\delta q}$ (independent of time) that is governed by the

signal-to-noise ratio of the continuous excitation. For these parameters, the total uncertainty estimates are of the form

$$q(t) = q_0 + \delta q(t) \pm \sigma_{\delta q}\,. \tag{9}$$

In summary, the total calibration uncertainty of $h(t)$ consists of systematic errors δq with known values, but the data is uncorrected for these errors. Future calibration of Advanced LIGO data will correct for these effects. The other source of uncertainty is statistical uncertainty, arising from uncertainty on the measured values, deviations from the modeled correction factors, and covariance of the fit to the measured data. In Secs. V, VI, and VII, we describe the models of each parameter in Q at the reference time t_0, and discuss estimates of statistical uncertainty σ_{q_0}, systematic error δq, and statistical uncertainty in the systematic error $\sigma_{\delta q}$. In Sec. VIII, we describe how the uncertainty and error estimates for these parameters are combined to estimate the overall accuracy and precision of the calibrated detector strain output $h(t)$.

IV. RADIATION PRESSURE ACTUATOR

The primary method for calibrating the actuation function A and sensing function C is an independent radiation pressure actuator called the *photon calibrator* (PC). A similar system was also used for calibration of the initial LIGO detectors [12].

Each detector is equipped with two photon calibrator systems, one for each end test mass, positioned outside the vacuum enclosure at the ends of the interferometer arms. For each system, 1047 nm light from an auxiliary, power-modulated, Nd^{3+}:YLF laser is directed into the vacuum envelope and reflects from the front surface of the mirror (test mass). The reflected light is directed to a power sensor located outside the vacuum enclosure. This sensor is an InGaAs photodetector mounted on an integrating sphere and is calibrated using a standard that is traceable to the National Institute of Standards and Technology (NIST) [13]. Power modulation is accomplished via an acousto-optic modulator that is part of an optical follower servo that ensures that the power modulation follows the requested waveform [14]. After modulation, the laser beam is divided optically and projected onto the mirror in two diametrically opposed positions. The spots are separated vertically, ±11.6 cm from the center of the optical surface, on the nodal ring of the drumhead elastic body mode, to minimize errors at high-frequency caused by bulk deformation [12, 15–17].

The laser power modulation induces a modulated displacement of the test mass that is given by [12]

$$x_{\mathrm{T}}^{(\mathrm{PC})}(f) = \frac{2P(f)}{c}\, s(f)\, \cos\theta \left(1 + \frac{M_{\mathrm{T}}}{I_{\mathrm{T}}}\, \vec{a}\cdot\vec{b}\right). \tag{10}$$

This modulated displacement is shown schematically on the left of Fig. 2. The terms entering this formula are as follows: f is the frequency of the power modulation, $P(f)$ is the power modulation amplitude, c is the speed of light, $s(f)$ is the mechanical compliance of the suspended mirror, $\theta \simeq 8.8^\circ$ is the angle of incidence on the mirror, $M_{\mathrm{T}} = 39.6\,\mathrm{kg}$ and $I_{\mathrm{T}} = 0.415\,\mathrm{kg\,m^2}$ are the mass and rotational moment of inertia of the mirror, and $\vec{a}$ and $\vec{b}$ are displacement vectors from the center of the optical surface to the photon calibrator center of force and the main interferometer beam, respectively. These displacements determine the amount of unwanted induced rotation of the mirror.

The compliance $s(f)$ of the suspended mirror can be approximated by treating the mirror as rigid body that is free to move along the optical axis of the arm cavity: $s(f) \simeq -1/[M_{\mathrm{T}}(2\pi f)^2]$. Cross-couplings between other degrees of freedom of the multi-stage suspension system, however, require that $s(f)$ be computed with a full, rigid-body model of the quadruple suspension. This model has been validated by previous measurements [18] and is assumed to have negligible uncertainty.

Significant sources of photon calibrator uncertainty include the NIST calibration of the reference standard (0.5%), self-induced test mass rotation uncertainty (0.4%), and uncertainty of the optical losses along the projection and reflection paths (0.4%). The overall 1σ uncertainty in the displacement induced by the photon calibrator, $x_{\mathrm{T}}^{(\mathrm{PC})}(f)$, is $\simeq 0.8\%$.

Measurements made during and after the observation period revealed that the estimate of $x_{\mathrm{T}}^{(\mathrm{PC})}$ includes systematic errors $\delta x_{\mathrm{T}}^{(\mathrm{PC})}$, resulting in frequency-independent correction factors of 1.013 and 1.002 for H1 and L1, respectively. These errors are combined with other known systematic errors in the response function uncertainty estimates as described in Sec. VIII.

V. ACTUATION FUNCTION CALIBRATION

The actuation strength for each suspension stage can be determined by comparing the interferometer's response to an excitation from the suspension stage actuator with one from the photon calibrator. The measured transfer function of the ith suspension stage actuation is given by

$$[\mathcal{K}_i A_i(f)]^{(\mathrm{meas})} = \frac{x_{\mathrm{T}}^{(\mathrm{PC})}(f)}{d_{\mathrm{err}}(f)} \times \frac{d_{\mathrm{err}}(f)}{\mathrm{exc}_i(f)}\,, \tag{11}$$

where $\mathrm{exc}_i(f)$ is the excitation applied to the ith stage ($i \in \{\mathrm{T}, \mathrm{P}, \mathrm{U}\}$).

Figs. 5 and 6 show the measured correction factors $q_{\mathrm{meas}}/q_0 = 1 + \delta q/q_0$ for the actuators of the lower three suspension stages of the H1 and L1 interferometers, and their corresponding systematic error estimates determined by low-order spline fits. As described in Sec. II, the actuation function, and therefore its uncertainty and error, only contribute significantly to the uncertainty estimate for h below ~45 Hz, which is the unity gain frequency for the differential arm length servo. While there are no data at frequencies above 100 Hz for H1, the L1 high-frequency data confirm that above 100 Hz, frequency-dependent deviations from the model are small.

There are larger frequency dependent errors in the models for the upper intermediate stages $\mathcal{K}_{\mathrm{U}} A_{\mathrm{U}}$ for both detectors. Recent measurements have shown that these result from unmodeled mechanical resonances as well as the non-negligible inductance of the electromagnetic coil actuators, which were not included in the model at the reference time. As shown in

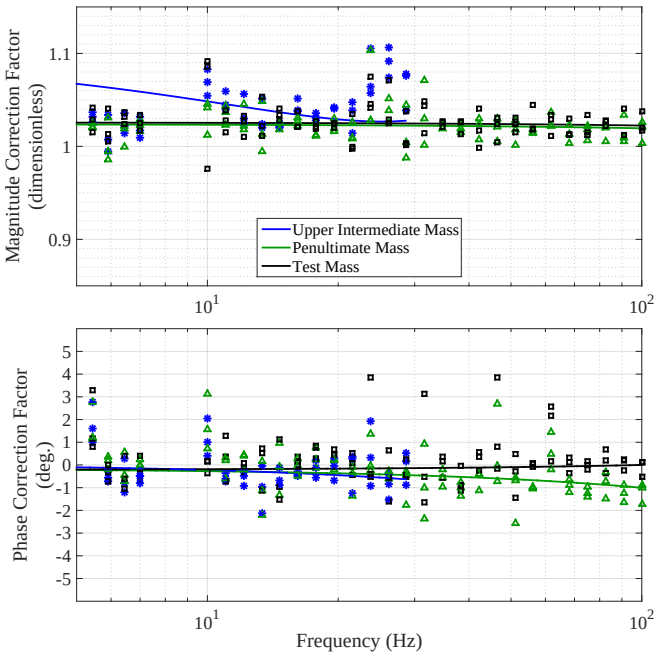

FIG. 5. Measured correction factors for the actuators of the lower three stages of the H1 suspension (symbols) and estimated systematic errors (solid lines) determined by low-order spline fits to the measured data. Only data up to 100 Hz for the bottom two stages were collected because the sensing function dominates the actuation function above ~45 Hz. Data for the upper intermediate mass is presented only up to 30 Hz because the actuation function for this stage is attenuated sharply above ~5 Hz.

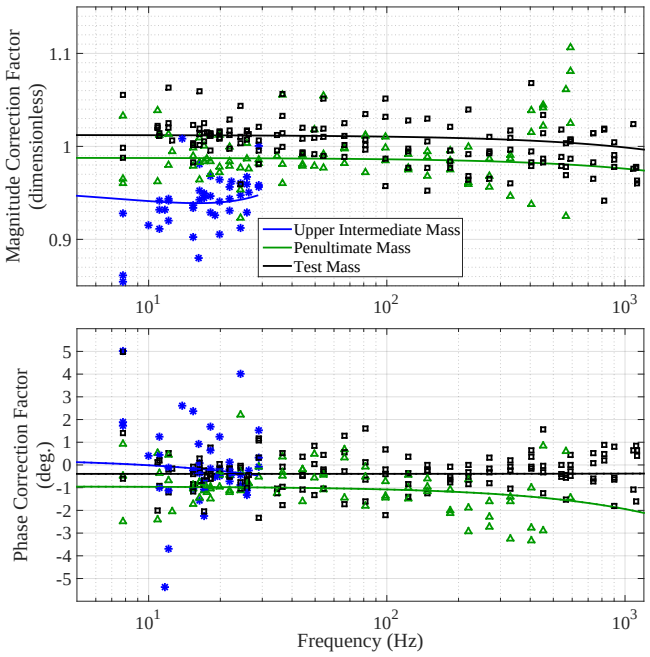

FIG. 6. Measured correction factors for the actuators of the lower three stages of the L1 suspension (symbols) and estimated systematic errors (solid lines) determined by low-order spline fits to the measured data. Data collected up to 1.2 kHz confirms the expected frequency dependence of the correction factors for the bottom two stages. Data for the upper intermediate mass is presented up to 30 Hz because the actuation function for this stage is attenuated sharply above ~5 Hz.

Fig. 4, however, the actuation strength of the upper intermediate mass is attenuated sharply above ~5 Hz by $F_{\rm U}$. It therefore does not substantially impact the overall actuation model in the relevant GW frequency band.

A systematic photon calibrator error would result in an overall error in the calibrated detector strain output. To investigate the possibility of such unknown systematic errors, two alternative calibration methods were employed. This is similar to what was done during initial LIGO [19]. One alternative method uses a radio-frequency oscillator reference and 532 nm laser light resonating in the interferometer arm cavities to calibrate the suspension actuators. The other method, which was also used during initial LIGO, uses the wavelength of the 1064 nm main laser light as a length reference. Their comparison with the photon calibrator is discussed in Appendix A. No large systematic errors were identified, but the accuracy of the alternate measurements is currently limited to ~10%.

VI. SENSING FUNCTION CALIBRATION

The sensing function can be measured using the photon calibrator (Sec. IV) and the calibrated suspension actuation system (Sec. V). The photon calibrator provides fiducial displacements $x_{\rm T}^{\rm (PC)}(f)$ and the interferometer response function is measured using the error signal $d_{\rm err}(f)$. The in-loop suspension actuation is used to measure $1 + G(f)$, where $G(f)$ is the open-loop transfer function of the differential arm length servo. Then the measured sensing function is given by

$$C^{\rm (meas)}(f) = [1 + G(f)] \times \frac{d_{\rm err}(f)}{x_{\rm T}^{\rm (PC)}(f)} \,. \tag{12}$$

Comparison with the sensing function model yields the measured correction factors for the sensing model, enabling estimation of systematic errors, and is shown in figure 7 for both H1 and L1. The smoothly varying sensing function systematic errors δC are significant only below 30 Hz. Below ~45 Hz, the unity gain frequency of the differential arm length servo, the impact of sensing function errors on the uncertainty in $h(t)$ is reduced because the actuation function is dominant in this frequency region (see Sec. II C).

VII. TIME-DEPENDENT SYSTEMATIC ERRORS

The scalar calibration parameters $\mathcal{K}_{\rm C}$, $f_{\rm C}$, and $\mathcal{K}_{\rm T}$ have been found to vary slowly as a function of time. Changes in these parameters are continuously monitored from the calibration lines observed in $d_{\rm err}$; these lines are injected via the photon calibrator and suspension system actuators. The amplitude of each calibration line is tuned to have a signal-to-noise ratio (SNR) of ~100 for a ten-second Fourier transform of $d_{\rm err}$. The calibration lines are demodulated, and their complex ratios are

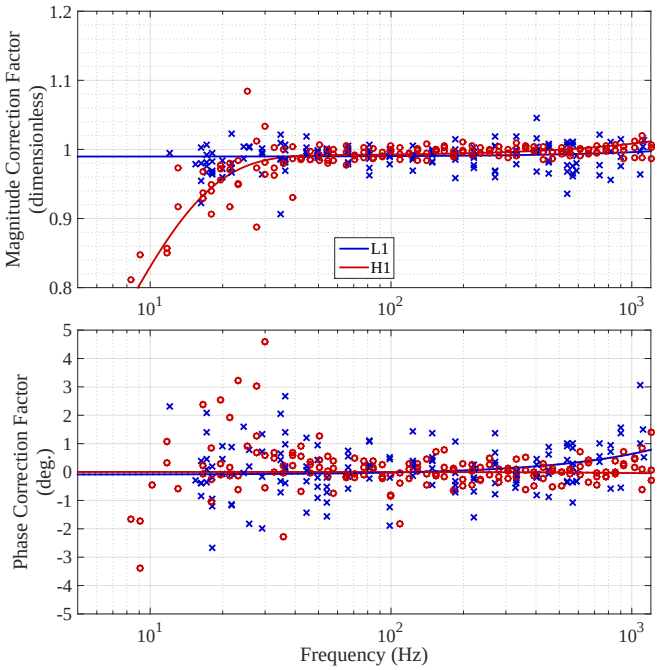

FIG. 7. Measured sensing function correction factors for L1 (blue crosses) and H1 (red circles) and estimated systematic errors (solid lines) determined by low-order spline fits to the measured data.

stored at a rate of 16 Hz. Running means of the complex ratios are computed over 128 s of this data, and are used to compute the scalar parameter as a function of time. The length of the running mean was chosen to reduce statistical uncertainty while still maintaining signal integrity for the chosen amplitudes, and to reduce the effect of non-Gaussian noise transients in the interferometer.

The optical parameters $\mathcal{K}_C$ and f_C change in response to variations in the alignment or the thermal state of the interferometer optics. The most dramatic changes occur over the course of the few minutes immediately after the interferometer achieves resonance, when the interferometer's angular control system is settling and the optics are coming into thermal equilibrium.

Variations in $\mathcal{K}_T$ occur due to the slow accumulation of stray ions onto the fused silica test mass [20, 21]. Test mass charging thus creates a slow change in the actuation gain, which takes several days to cause an observable change. The upper stage actuation gains, $\mathcal{K}_P$ and $\mathcal{K}_U$, are also monitored, but the measurements do not show time-dependent variations that are larger than the precision of the tracking measurements.

Time-dependent changes in the gains $\mathcal{K}_i$ are represented by relative, dimensionless correction factors, $\kappa_i(t) = 1 + \delta\mathcal{K}_i(t)/\mathcal{K}_i$. Changes in the pole frequency, however, are reported as an absolute change: $f_C(t) = f_C + \delta f_C$. The frequency-dependent correction factor to $C^{(\mathrm{model})}(f)$, resulting from errors in f_C, is determined by taking the ratio of two normalized, single-pole transfer functions, one with f_C at the reference time and the other with f_C at the time of relevant observational data. All time-dependent errors also have statistical uncertainty, which is included in $\sigma_{\delta q}$. These uncertainties arise from the limited SNR of the calibration lines in the computed Fourier transforms of d_{err}.

TABLE II. Dimensionless correction factors κ_i and systematic error in cavity pole frequency, and their associated statistical uncertainties (in parenthesis) during GW150914.

	H1		L1	
	Mag.	Phase (deg.)	Mag.	Phase (deg.)
κ_T	1.041(2)	−0.7(1)	1.012(2)	−1.2(1)
κ_{PU}	1.022(2)	−1.3(2)	1.005(3)	−1.5(2)
κ_C	1.001(3)	N/A	1.007(3)	N/A
δf_C (Hz)	−8.1(1.4)	N/A	0.5(1.9)	N/A

Measurements to be used as references for the interferometer models were made 3 days prior and 1 day prior to GW150914 at H1 and L1, respectively. Since the charge accumulation on the test mass actuators is slow, any charge-induced changes in the test mass actuation function parameters during these few days was less than 1%. At the time of GW150914, H1 had been observing for 2 hours and L1 had been observing for 48 minutes, so both detectors had achieved stable alignment and thermal conditions. We thus expect that sensing function errors were also very small, though they fluctuate by a few percent around the mean value during normal operation. The correction factors measured at the time of GW150914 are representative of the factors recorded for the 38 day observational period and are shown in Table II.

VIII. ESTIMATE OF TOTAL UNCERTAINTY

The total statistical uncertainty of the model parameters are combined to form the total statistical uncertainty of the response function (Eq. 5) σ_R, and is given by

$$\sigma_R^2(f) = \sum_{q\in Q}\left[\frac{\partial R(f)}{\partial q}\right]^2\left[\sigma_{q_0}^2(f) + \sigma_{\delta q}^2(f)\right], \qquad (13)$$

where $\partial R(f)/\partial q$ is the partial derivative of R with respect to a given parameter q. The systematic error of the response function δR is evaluated by computing the ratio of the response function with its parameters evaluated with and without known and measured systematic errors

$$1 + \frac{\delta R(f,t)}{R(f)} = \frac{R(f,t\,;q_1+\delta q_1, q_2+\delta q_2,\ldots,q_n+\delta q_n)}{R(f\,;q_1,q_2,\ldots,q_n)}. \qquad (14)$$

Therefore, the response function correction quantifies the error of the calibrated detector strain output for any time t.

Figure 8 shows the total statistical uncertainty and systematic errors in the response function $R(f)$ at the time of GW150914 and defines the limit of the precision and accuracy of $h(t)$. Systematic errors at low frequency are dominated by the systematic errors in the actuation function, whereas at high frequencies, the systematic error is dominated by the sensing function systematic error. The frequency dependence of the sensing and actuation models, and of the uncertainties presented here, is expected to be smoothly varying in the 20 Hz to 1 kHz band.

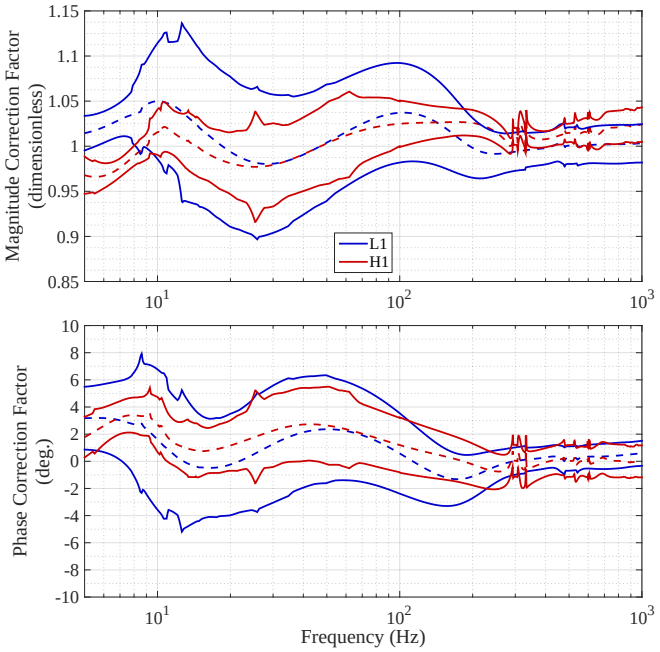

FIG. 8. Known systematic error and uncertainty for the response function $R(f)$ at the time of GW150914, expressed as a complex correction factor $1+\delta R(f,t)/R(f)$. The upper panel shows the magnitude, and the lower panel shows the phase. Dashed lines in each subplot indicate the nominal value (i.e., systematic error) of the correction factor, which accounts for known systematic errors $\{\delta q\}$ in the model parameters. The solid lines are the total statistical uncertainty σ_R surrounding the systematic error which define the limits of the precision and accuracy of our estimate of $h(t)$.

For all frequencies relevant to GW150914, between 20 Hz and 1 kHz, the uncertainty is less than 10% in magnitude and 10° in phase. The comparison of measurements with models presented in Sec. V and Sec. VI of this paper are consistent with that expectation.

IX. INTER-SITE TIMING ACCURACY

Digital signals $d_{\rm err}$ and $d_{\rm ctrl}$ are derived from signals captured by analog-to-digital converters as a part of the LIGO data acquisition system [22] and are stored in a mass data storage system which records these signals for later analysis. The LIGO timing system [23] provides the reference timing information for the data acquisition system.

Each detector's timing system uses a single Trimble Thunderbolt E GPS receiver as the timing reference. Additional GPS receivers and one cesium atomic clock serve as witness clocks to independently monitor the functionality of the main GPS reference. Once a second, timing comparators monitor the clock edge differences (modulo one second) between the main GPS receiver and the witness clocks with sub-microsecond accuracy. We did not observe any anomaly at the time of GW150914.

As a check of relatively large absolute timing offset, two witness GPS units at each site produce IRIG-B time code signals which are recorded by the data acquisition system. IRIG-B time code maps the GPS time onto the Coordinated Universal Time (UTC). Comparison of the IRIG-B time code and the data acquisition time stamp of the recorded signal allows us to measure any large time offset which cannot be measured by the timing comparators. At the time of GW150914, IRIG-B witness signals were available at H1. At L1, IRIG-B signals generated by the timing system itself were recorded as a self-consistency check at the time of GW150914. Later into the O1 run, the L1 IRIG-B witness signals were added. Throughout all 38 days of observation, no inconsistency was observed between any of recorded IRIG-B signals and the data time stamps.

Additional monitoring is performed to measure any potential timing offset between the timing system and the analog-to-digital converters. Analog diagnostic signals with a known waveform are generated by the timing system and injected into a subset of analog-to-digital converters. The diagnostic signals on the units most directly related to the estimated detector strain $h(t)$—the ones of the photon calibrator readback sensor and of the GW readout photodetectors—are recorded and analyzed. The time offset of the recorded waveform is compared against the expected delay, where any discrepancy would reveal a single analog-to-digital converter's deviation relative to the timing system. This comparison was performed over a 10-minute window centered on the time of detection. In both detectors, all offsets were only 0.6 to 0.7 µs on average, with the standard deviation smaller than 1 ns and without any significant outliers. Although potential timing offsets between different channels on the same analog-to-digital-converter board were not measured, there is no reason to believe that there were any timing offsets larger than a few microseconds.

The time offset of each LIGO detector also depends on the offset of the main GPS receiver relative to the common time frame, i.e., UTC. We expect this typically to be smaller than 1 µs based on the conservative estimate of the GPS specification [24] as well as the comparator and IRIG-B measurements.

Based on these observations we conclude that the LIGO timing systems at both sites were working as designed and internally consistent over all 38 days of observation. Even if we use the most conservative estimate as a measure of caution, we conclude that the absolute timing offsets from UTC at both sites were no larger than 10 µs.

X. IMPACT OF CALIBRATION UNCERTAINTIES ON GW150914

The total uncertainty in $h(t)$ reported in Section VIII is less than 10% in magnitude and 10° in phase from 20 Hz to 1 kHz for the entire 38 calendar days of observational data during which GW150914 was observed. The astrophysical searches used for detecting events like GW150914 are not limited by this level of calibration uncertainty [25, 26].

Calibration uncertainties directly affect the estimation of the source parameters associated with events like GW150914. The amplitude of the gravitational wave depends on both the luminosity distance and the orbital inclination of the source, so

uncertainty in the magnitude of the calibration, determined by the photon calibrator, directly affects the estimation of the luminosity distance. The luminosity distance also depends strongly, however, on the orbital inclination of the binary source, which is poorly constrained by the two nearly co-aligned Advanced LIGO detectors. Thus, the 10% uncertainty in magnitude does not significantly degrade the accuracy of the luminosity distance for GW150914 [27]. The absolute scale is cross-checked with two additional calibration methods, one referenced to the main laser wavelength and another referenced to a radio-frequency oscillator (Appendix A). Each method is able to confirm the scale at the 10% level in both detectors, comparable to the estimate of total uncertainty in absolute scale.

An uncertainty of 10% in the absolute strain calibration results in a ∼30% uncertainty on the inference of coalescence rate for similar astrophysical systems [28]. Since the counting uncertainty inherent in the rate estimation surrounding GW150914 is larger than the 30% uncertainty in rates induced by the calibration uncertainty, the latter does not yet limit the rate estimate.

All other astrophysical parameters rely on the accuracy of each detector's output calibration as a function of frequency. The physical model of the frequency dependence underlying this uncertainty was not directly available to the parameter estimation procedure at the time of detection and analysis of GW150914. Instead, a preliminary model of the uncertainty's frequency dependence was used, the output of which was a smooth, parameterized shape over the detection band [27, 29]. The parameters of the preliminary model were given Gaussian prior distributions such that its output was consistent with the uncertainties described in this paper. Comparison between the preliminary model and the physical model presented in this paper have shown that the preliminary model is sufficiently representative of the frequency dependence. In addition, its uncertainty has been shown not to limit the estimation of astrophysical parameters for GW150914 [27].

Estimating the sky-location parameters depends partially on the inter-site accuracy of the detectors' timing systems [30]. These systems, and the consistency checks that were performed on data containing GW150914, are described briefly in Section VI. The absolute time of detectors' data streams is accurate to within 10 µs, which does not limit the uncertainty in sky-location parameters for GW150914 [27, 31].

XI. SUMMARY AND CONCLUSIONS

In this paper, we have described how the calibrated strain estimate $h(t)$ is produced from the differential arm length readout of the Advanced LIGO detectors. The estimate is formed from models of the detectors' actuation and sensing systems and verified with calibrated, frequency-dependent excitations via radiation pressure actuators at reference times. This radiation pressure actuator relies on a NIST-traceable laser power standard and knowledge of the test mass suspension dynamics, which are both known at the 1% level. The reference and subsequent confirmation measurements inform the static, frequency-dependent systematic error and statistical uncertainty in the estimate of $h(t)$. Time-dependent correction factors to certain model parameters are monitored with single-frequency excitations during the entire observation period. We report that the value and statistical uncertainty of these time-dependent factors are small enough that they do not impact astrophysical results throughout the period from September 12 to October 20, 2015.

The reference measurements and time-dependent correction factors are used to estimate the total uncertainty in $h(t)$, which is less than 10% in magnitude and 10° in phase from 20 Hz to 1 kHz for the entire 38 calendar days of observation during which GW150914 was observed. This level of uncertainty does not significantly limit the estimation of source parameters associated with GW150914. We expect these uncertainties to remain valid up to 2 kHz once the forthcoming calibration for the full LIGO observing run is complete.

Though not yet the dominant source of error, based on the expected sensitivity improvement of Advanced LIGO [32], calibration uncertainties may limit astrophysical measurements in future observing runs. In the coming era of numerous detections of gravitational waves from diverse sources, accurate estimation of source populations and properties will depend critically on the accuracy of the calibrated detector outputs of the advanced detector network. In the future, the calibration physical model and its uncertainty will be directly employed in the astrophysical parameter estimation procedure, which will reduce the impact of this uncertainty on the estimation of source parameters. We will continue to improve on the calibration accuracy and precision reported here, with the goal of ensuring that future astrophysical results are not limited by calibration uncertainties as the detector sensitivity improves and new sources are observed.

ACKNOWLEDGMENTS

The authors gratefully acknowledge the support of the United States National Science Foundation (NSF) for the construction and operation of the LIGO Laboratory and Advanced LIGO as well as the Science and Technology Facilities Council (STFC) of the United Kingdom, the Max-Planck-Society (MPS), and the State of Niedersachsen/Germany for support of the construction of Advanced LIGO and construction and operation of the GEO600 detector. Additional support for Advanced LIGO was provided by the Australian Research Council. The authors gratefully acknowledge the Italian Istituto Nazionale di Fisica Nucleare (INFN), the French Centre National de la Recherche Scientifique (CNRS) and the Foundation for Fundamental Research on Matter supported by the Netherlands Organisation for Scientific Research, for the construction and operation of the Virgo detector and the creation and support of the EGO consortium. The authors also gratefully acknowledge research support from these agencies as well as by the Council of Scientific and Industrial Research of India, Department of Science and Technology, India, Science & Engineering Research Board (SERB), India, Ministry of Human Resource Development, India, the Spanish Ministerio de Economía y Competitividad, the Conselleria d'Economia i

Competitivitat and Conselleria d'Educació, Cultura i Universitats of the Govern de les Illes Balears, the National Science Centre of Poland, the European Union, the Royal Society, the Scottish Funding Council, the Scottish Universities Physics Alliance, the Lyon Institute of Origins (LIO), the National Research Foundation of Korea, Industry Canada and the Province of Ontario through the Ministry of Economic Development and Innovation, the National Science and Engineering Research Council Canada, the Brazilian Ministry of Science, Technology, and Innovation, the Research Corporation, Ministry of Science and Technology (MOST), Taiwan and the Kavli Foundation. The authors gratefully acknowledge the support of the NSF, STFC, MPS, INFN, CNRS and the State of Niedersachsen/Germany for provision of computational resources. This article has been assigned the LIGO document number P1500248.

Appendix A: Photon calibrator cross-check

It is essential to rule out large systematic errors in the photon calibrator by comparing it against fundamentally different calibration methods. For Advanced LIGO, two alternative methods have been implemented. One is based on a radio-frequency oscillator and the other based on the laser wavelength. Each of them is described below.

1. Calibration via radio-frequency oscillator

As part of the control sequence to bring the interferometer to resonance, the differential arm length is measured and controlled using two auxiliary green lasers with a wavelength of 532 nm [2, 33, 34]. Although designed as part of the interferometer controls, this system can provide an independent measure of the differential arm length.

The two green lasers are offset from each other in frequency by 158 MHz. The frequency of each is independently locked to one of the arm cavities with a control bandwidth of several kilohertz. Therefore, the frequency fluctuations of each green laser are proportional to the length fluctuations of the corresponding arm cavity through the relation $\Delta\nu_g/\nu_g \approx \Delta L/L$, where ν_g is the frequency of either of the auxiliary lasers [35]. Beams from these two lasers are interfered and measured on a photodetector, producing a beat-note close to 158 MHz. As the differential arm length varies, the beat-note frequency shifts by the amount defined by the above relation. This shift in the beat-note frequency is converted to voltage by a frequency discriminator based on a voltage controlled oscillator at a radio frequency. Therefore the differential arm length can be calibrated into physical displacement by calibrating the response of the frequency discriminator.

A complicating factor with this method is the limited availability. This method is only practical for calibration in a high noise interferometer configuration because sensing noise is too high. Another set of measurements is thus required to relate the high noise actuators to the ones configured for low noise observation. These extra measurements are conducted in low noise interferometer state where both high and low noise actuators are excited. Since both excitations are identically suppressed by the control system, simply comparing their responses using the readout signal $d_{\rm err}$ allows for propagation of the calibration. In summary, one can provide an independent calibration of every stage of the low noise actuator by three sets of measurements:

$$[\mathcal{K}_i A_i(f)]^{(\rm rf)} = \left(\frac{\Delta L}{\mathrm{exc}_{\rm HR}(f)}\right) \times \left(\frac{\mathrm{exc}_{\rm HR}(f)}{d_{\rm err}(f)}\right) \times \left(\frac{d_{\rm err}(f)}{\mathrm{exc}_i(f)}\right), \quad \text{(A1)}$$

where $\mathrm{exc}_{\rm HR}$ is digital counts applied to excite a high noise actuator. The first term on the right hand side represents the absolute calibration of the high noise actuator, and the final two ratios represent the propagation of the calibration in low noise interferometer state.

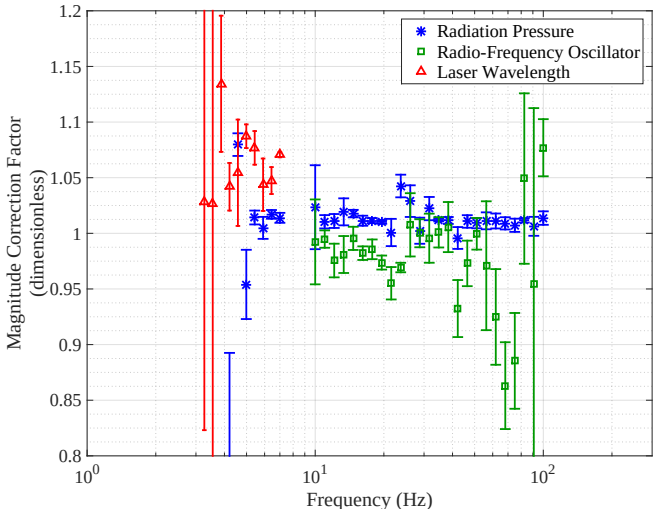

FIG. 9. Comparison between radiation pressure, radio frequency oscillator, and laser wavelength calibration techniques, displayed as $[\mathcal{K}_T A_T(f)]^{(\rm method)}/[\mathcal{K}_T A_{T(f)}]^{(\rm model)}$, for the test mass stage of the H1 interferometer. Only statistical uncertainty is shown; systematic errors for individual methods are not shown.

2. Calibration via laser wavelength

The suspension actuators can be calibrated against the main laser wavelength ($\lambda_r = 1064$ nm) using a series of different optical topologies. The procedure is essentially the same as the procedure for initial gravitational wave detectors [36, 37].

First, the input test masses and the beamsplitter are used to form a simple Michelson topology, which allows the input test mass suspension actuators to be calibrated against the main laser wavelength. Then, a laser (either main or auxiliary green) is locked to the Fabry–Pérot cavity formed by the X-arm input and end test masses. This allows the end test mass actuators to be calibrated against the corresponding input test mass actuators. Finally, in the full optical configuration, the low noise suspension actuators (of the Y-arm end test mass) are calibrated against the X-arm end test mass suspension actuators.

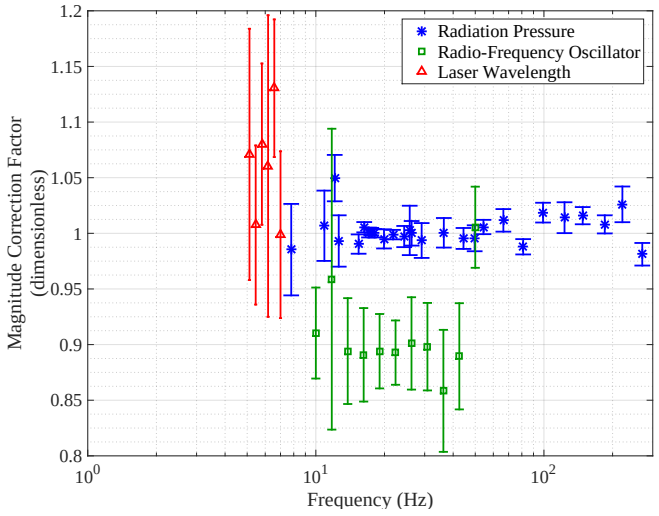

FIG. 10. Comparison between radiation pressure, radio frequency oscillator, and laser wavelength calibration techniques, displayed as $[\mathcal{K}_{\rm T}A_{\rm T}(f)]^{\rm (method)}/[\mathcal{K}_{\rm T}A_{\rm T(}f{\rm)}]^{\rm (model)}$, for the test mass stage of the L1 interferometer. Only statistical uncertainty is shown; systematic errors for individual methods are not shown.

In Advanced LIGO, one practical drawback is the narrow frequency range in which this technique is applicable. Not all input test masses suspensions have actuation on the final stage, so the the penultimate mass suspension actuators must be used instead. This limits the frequency range over which one can drive above the displacement sensitivity of the Michelson. The penultimate stage actuators themselves are also weak, further reducing the possible signal-to-noise ratio of the fundamental measurement. As a consequence, the useable frequency range is limited to below 10 Hz.

3. Results and discussion

Figures 9 and 10 show the correction factor for $\mathcal{K}_T A_T$. Only the test mass stage is shown for brevity. This comparison was done for all three masses of actuation system and show similar results. With the correction factors of both independent methods (radio frequency oscillator and laser wavelength) within 10% agreement with that as estimated by radiation pressure (again, for all stages of actuation), we consider the absolute calibration of the primary method confirmed to that 10% level of accuracy. At this point, the independent methods are used merely to bound the systematic error on the radiation pressure technique's absolute calibration; considerably less effort and time were put into ensuring that all discrepancies and systematic errors within the independent method were well-quantified and understood. Only statistical uncertainty—based on coherence for each compound-measurement point in each method—is shown, because the systematic error for these independent methods have not yet been identified or well-quantified. Refinement and further description of these techniques is left for future work.

[1] B. Abbott *et al.*, Phys. Rev. Lett. **116**, 061102 (2016), https://dcc.ligo.org/LIGO-P150914/public/main.
[2] The LIGO Scientific Collaboration, Classical Quant. Grav. **32**, 074001 (2015).
[3] T. T. Fricke *et al.*, Classical Quant. Grav. **29**, 065005 (2012).
[4] X. Siemens, B. Allen, J. Creighton, M. Hewitson, and M. Landry, Classical Quant. Grav. **21**, S1723 (2004).
[5] J. Mizuno *et al.*, Phys. Lett. A **175**, 273 (1993).
[6] M. Rakhmanov, J. D. Romano, and J. T. Whelan, Classical Quant. Grav. **25**, 184017 (2008).
[7] N. A. Robertson *et al.*, Classical Quant. Grav. **19**, 4043 (2002).
[8] S. M. Aston *et al.*, Classical Quant. Grav. **29**, 235004 (2012).
[9] F. Matichard *et al.*, Classical Quant. Grav. **32**, 185003 (2015).
[10] A. Buonanno and Y. Chen, Phys. Rev. D **65**, 042001 (2002).
[11] J. S. Bendat and A. G. Piersol, *Random data: analysis and measurement procedures*, Vol. 729 (John Wiley & Sons, 2011).
[12] E. Goetz *et al.*, Classical Quant. Grav. **26**, 245011 (2009).
[13] D. Tuyenbayv *et al.*, (2015), https://dcc.ligo.org/LIGO-T1500283/public.
[14] R. L. Savage Jr *et al.*, (2014), https://dcc.ligo.org/LIGO-T1300442/public.
[15] J. R. Hutchinson, J. Appl. Mech. **47**, 901 (1980).
[16] S. Hild *et al.*, Classical Quant. Grav. **24**, 5681 (2007).
[17] H. P. Daveloza *et al.*, *Journal of Physics: Conference Series*, **363**, 012007 (2012).
[18] B. Shapiro, M. Barton, N. Mavalvala, R. Mittleman, and K. Youcef-Toumi, Mechatronics, IEEE/ASME Transactions on **20**, 13 (2015).
[19] E. Goetz *et al.*, Classical Quant. Grav. **27**, 084024 (2010).
[20] L. Carbone *et al.*, Classical Quant. Grav. **29**, 115005 (2012).
[21] M. Hewitson *et al.*, Classical Quant. Grav. **24**, 6379 (2007).
[22] R. Bork *et al.*, in *Proc. of Industrial Control And Large Experimental Physics Control System (ICALEPSC) conference* (2011).
[23] I. Bartos *et al.*, Classical Quant. Grav. **27**, 084025 (2010).
[24] *Interface Specification IS-GPS-200H*, Tech. Rep. (Global Positioning Systems Directorate, 2014).
[25] B. Abbott *et al.*, (2016), https://dcc.ligo.org/LIGO-P1500229/public/main.
[26] B. Abbott *et al.*, (2016), https://dcc.ligo.org/LIGO-P1500269/public/main.
[27] B. Abbott *et al.*, (2016), https://dcc.ligo.org/LIGO-P1500218/public/main.
[28] B. Abbott *et al.*, (2016), https://dcc.ligo.org/LIGO-P1500217/public/main.
[29] W. Farr, B. Farr, and T. Littenberg, https://dcc.ligo.org/LIGO-T1400682/public.
[30] S. Fairhurst, New J. Phys. **11**, 123006 (2009).
[31] B. Abbott *et al.*, (2016), https://dcc.ligo.org/LIGO-P1500227/public/main.
[32] B. P. Abbott, others (LIGO Scientific Collaboration, and V. Collaboration), Living Rev. Relativity **19** (2016).
[33] A. Staley *et al.*, Classical Quant. Grav. **31**, 245010 (2014).
[34] A. Mullavey *et al.*, Opt. Express **20**, 81 (2012).
[35] K. Izumi *et al.*, J. Opt. Soc. Am. A **29**, 2092 (2012).
[36] T. Accadia *et al.*, Classical Quant. Grav. **28**, 025005 (2011).
[37] J. Abadie *et al.*, Nucl. Instrum. Meth. A **624**, 223 (2010).